Journal of Materials Chemistry C

Accepted Manuscript

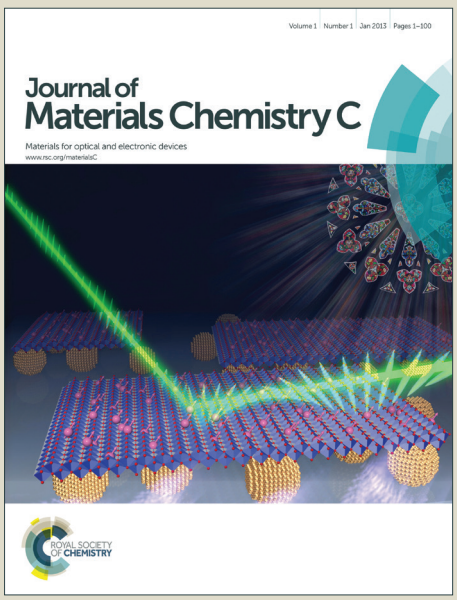

ROYAL SOCIETY OF CHEMISTRY

www.rsc.org/materialsC

Journal Name

RSCPublishing

ARTICLE

Core-satellite $BaTiO_3$@$SrTiO_3$ assemblies for local compositionally graded relaxor ferroelectric capacitor with enhanced energy storage density and high energy efficiency

Cite this: DOI: 10.1039/x0xx00000x

Received 00th January 2012,
Accepted 00th January 2012

DOI: 10.1039/x0xx00000x

www.rsc.org/

Longwen Wu, Xiaohui Wang,* Huiling Gong, Yanan Hao, Zhengbo Shen and Longtu Li*

Dielectric capacitors with high energy density and low energy loss are of great importance in high power electric and electronic systems. Traditional $BaTiO_3$ (BT) or its solid solutions have been widely explored as high energy density materials owing to their notably high dielectric constant. However, these materials often suffer from significant drawbacks of strong dielectric nonlinearity, low breakdown strength and high hysteresis loss, limiting the energy storage density and energy utilization efficiency. In this study, by using core-satellite structured nanocubic $SrTiO_3$ (ST) decorated BT assemblies, a composite capacitor with enhanced breakdown strength and weaker dielectric nonlinearity was successfully fabricated in contrast with the pure ferroelectric BT ceramic, resulting in elevated energy storage density and high energy efficiency as extracted from the polarization-electric field loops. The mechanism behind the improved electric and dielectric performances was discovered to be the remarkable supression of grain size owing to the existence of the ST nanocubes and also the ferroelectric relaxor behaviors arising from the local compositionally graded structure due to the controlled sintering and modulated diffusion of Sr element. This work provided a new approach for fabrication of dielectric materials with promising high energy density and low loss.

Introduction

Global environmental pollution, energy depletion and world climate change have been causing people's ever-increasing concern. Various kinds of new and clean energy generation technologies, such as solar, wind and thermal energy utilization are being developed, which are meant for replacing the non-renewable fossil fuels. In company with such kinds of energy generation, the energy storage technologies are urgently demanded for efficient utilization of the power produced from these renewable sources.[1, 2] The most ideal energy storage devices will be of high power density, high energy density and low cost.[3] Capacitors which intrinsically possess high power density and fast charge/discharge capability are promising candidates for energy storage devices. Compared with other technologies, they are also of lower cost, more thermally stable and mechanically robust.[4] Besides, those made of dielectrics, including polymers and ceramics, are widely proposed for commercial, consumer, medical and military use in high power systems such as filtering, voltage smoothing, snubbing, coupling and decoupling, power-conditioning, electromagnetic interference (EMI) suppression, medical defibrillators, electric armor and gun, direct energy weapon, *etc*.[5-8] In recent years, towards the miniaturization, light weight and integration of electric and electronic devices, capacitors with high energy storage density are becoming distinctly important.[7, 9]

Mathematically, energy storage density for ideal linear dielectrics is linearly proportional to its permittivity and quadratically proportional to its breakdown strength. However, for nonlinear dielectrics, the energy storage density is also restricted by their nonlinear polarization behaviors, remanent polarizations and hysteresis losses. At present, dielectrics for energy storage under heated research can mainly be divided into four categories: polymer or polymer-based composites[10-16], dielectric glass-ceramics,[17] antiferroelectrics,[9, 18, 19] and relaxor ferroelectrics.[3, 20] In the midst of them, relaxor ferroelectrics with the advantages of slim hysteresis and low remanent polarization which provide high electric displacement, low loss and weakened dielectric nonlinearity are receiving growing interest in storing energy with fast discharge capacity.[3, 6, 10, 20, 21] For example, $Pb(Zn_{1/3}Nb_{2/3})O_3$-$Pb(Mg_{1/3}Nb_{2/3})O_3$-$PbTiO_3$ (PZN-PMN-PT) relaxor thin films prepared by Yao, *et al*.[21] showed a large maximum polarization of 108 $\mu C/cm^2$, and a

moderate remanent polarization of 20 μC/cm^2 at 700 kV/cm, resulting in an energy storage density of 15.8 J/cm^3. Kwon and co-authors[22] studied the energy storage performance in $BaTiO_3$-$Bi(Mg, Ti)O_3$ thin films, which exhibited nearly linear polarization response and the energy storage density was found to be as high as 37 J/cm^3 at 1.9 MV/cm. Ogihara, *et al*.[6] found that $0.7BaTiO_3$-$0.3BiScO_3$ ceramic was of high and temperature-stable dielectric constant and was feasible for energy storage capacitors at elevated temperatures. Besides, an energy storage density for a single dielectric layer was discovered to be about 6.1 J/cm^3 at a field of 73kV/mm at room temperature.

Recently, BT or its solid solutions have received dramatic attentions concerning the applications in the field of energy storage by virtue of their high dielectric constant.[23-26] However, these materials often have significant weaknesses of strong dielectric nonlinearity, low breakdown strength and high hysteresis loss, hindering the energy storage density and energy utilization efficiency. Strontium titanate, as quantum paraelectrics, has the intrinsic nature of high breakdown strength and weak dielectric nonlinearity irrespective of its moderate permittivity.[27-29] An idea capturing our mind is to combine the complementary merits of BT with ST to get a superimposed effect. Additionally, remarkable modifications of the properties of functional materials can be acquired by locally altering periodic chemical composition fluctuations.[30] A good example is the commonly seen "core-shell" structure tuning in multilayer ceramic capacitor industry, where the ceramic grain structure can be modified through careful doping and sintering. Bulk material or thin films with local compositionally graded structure were reported to have performance superior to homogeneous solid solutions or separate components.[30-32]

In this work, by first preparation of core-satellite $BaTiO_3$@$SrTiO_3$ (BT@ST) assemblies through a facile sol-precipitation approach, and then followed by careful control of sintering, herein we report a novel strategy for fabrication of relaxor ferroelectric capacitor with local compositionally graded structure. The dielectric nonlinearity of the BT@ST bulk ceramic was found to be weakened, while simultaneously the breakdown strength of which was improved, resulting in enhanced energy storage density and improved energy efficiency compared with the pure BT ceramic. The mechanisms leading to the resulted superior performances were also explored and discussed.

Experimental

The BT particles with an average diameter of ~100 nm were supplied by Sakai Chemical Industry Co., Ltd, Japan. Titanate coupling agent (Product NO. TC-2) was purchased from Taichang Chemical Co., Ltd (Anhui, China). Strontium hydroxide octahydrate [$Sr(OH)_2{\cdot}8H_2O$; 99%] was received from Alfa Aesar Chemical Co., Ltd, USA. Tetrabutyl titanate [$Ti(OC_4H_9)_4$; 99%], triethylene glycol (TEG, 99%), ammonia ($NH_3{\cdot}H_2O$; 25-28%) and other chemical reagents were obtained from Sinopharm Chemical Reagent Company (Beijing, China). Deionized water was utilized throughout the experiments, and all the chemicals were used as received without further treatment.

The core-satellite BT@ST assemblies were synthesized *via* a sol-precipitation approach. Firstly, 5 g BT particles were added into 150 ml TEG in a three-necked round-bottomed flask, and then the mixture was stirred for 30 min at room temperature. For surface modification, several drops of TC-2 were added and the suspension was stirred for 1 h, prior to which a small amount of water was added to facilitate the pre-hydrolysis of the coupling agent. After that, 2.0 g $Sr(OH)_2{\cdot}8H_2O$ was added as the strontium source, followed by the addition of about 10 ml $NH_3{\cdot}H_2O$. To prevent abrupt hydrolysis, 2.6 ml $Ti(OC_4H_9)_4$ was drop-wisely added, and finally, the mixture was refluxed at 160 ℃ for 24 h. The formed precipitates were washed with deionized water and ethanol both for three times and centrifugated at 4000 rpm for 4 min to ensure the removal of the solvent and unreacted reagents. The obtained BT@ST powders were dried at 80 ℃ overnight and recovered in a desiccator for further use. The schematic of the preparation process of the BT@ST powders is demonstrated in Fig. 1. For the fabrication of bulk ceramic, the as-synthesized powders were mixed with polyvinyl alcohol binder and pressed into pellets, followed by conventional sintering at 1250 ℃ for 4 h under the ambient atmosphere. Bulk ceramics of pure BT are also fabricated and tested under the same conditions for comparison.

The phase structures of the BT and BT@ST powders and bulk ceramics were determined by X-ray diffraction (XRD; Bruker D8 Advance A25, Germany) with Cu Kα radiation (λ = 1.5406 Å) operated at 40 kV and 200 mA. The Fourier transform infrared (FT-IR) spectra were recorded using an FT-IR spectrometer (Vertex 70v, Bruker Ltd., Germany). Thermogravimetric (TG) and differential scanning calorimetry (DSC) analysis were conducted with a TG/DSC instrument (STA 409PC, Netzsch, Selb, Germany). Transmission electron microscopy (TEM), high-resolution transmission electron microscopy (HR-TEM) images and selected-area electron diffraction (SAED) patterns were obtained through high-resolution transmission electron microscopes (JEM-2010, JEOL Ltd., Tokyo, Japan and Tecnai G^2 20, FEI, USA). Energy dispersive spectroscopy (EDS) was carried out on X-ray energy-dispersive spectrometer systems (Oxford Instruments, UK) equipped on a transmission electron microscope (Tecnai G^2 F20, FEI, USA). Morphologies of the samples were observed with a scanning electron microscope (MERLIN VP Compact, Carl Zeiss, Germany). For electrical measurements, the sintered ceramics were polished and then coated with silver paste for both sides. DC bias and leakage current properties were measured under the Capacitance-Voltage (C-V) and Current-Voltage (I-V) mode respectively on a power device analyzer/curve tracer (B1505A, Agilent Technologies, USA). Dielectric response was employed with an impedance analyzer coupled with a temperature controller (Novocontrol Technologies GmbH & Co. KG, Germany) in the frequency range of 100 Hz to 10^6 Hz under temperatures varying from -60-150 ℃. The dielectric breakdown strength test was

performed on a withstanding voltage tester (YD2013, Changzhou Yangzi Electronic Co., Ltd, China) by bathing the samples in silicon oil. Polarization-electric field (P-E) hysteresis loops were measured using a Radiant precision workstation (RT6000HVA, Radiant Technologies, Northford, Connecticut, USA) based on a Sawyer-Tower circuit at room temperature and 1 Hz.

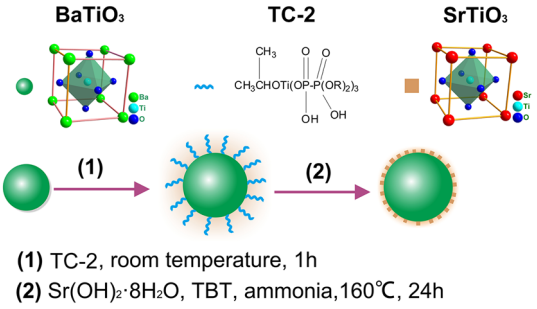

Fig. 1 Schematic of the preparation process of core-satellite BT@ST assemblies.

Results and discussion

Strontium titanate tends to crystallize independently in the solution rather than deposit on the surface of BT particles from experimental experience. To solve this problem, titanate coupling agent TC-2 is employed so as to activate the surface of BT particles for the growth of ST. The molecular structure of TC-2 is illustrated in Fig. 1. As shown in Fig. 1, the TC-2 molecule can primarily be divided into two functional zones. One is the organo-titanate end, which is analogous to that of $Ti(OC_4H_9)_4$ and may serve as the growth point of the ≡Ti-O-Ti≡ network. The other is the organophosphate group, which is intended to bind the surface of BT particles. As demonstrated in Fig. 2, a uniform layer with an average thickness of ~6 nm is successfully formed on the surface of BT particles due to the hydrolysis of TC-2, revealing good treatment effect. The binding mechanism of TC-2 to the surface of BT particles can be inferred from the disparities of the FT-IR spectra before and after surface modification as shown in Fig. 3. The peaks at 2935 cm^{-1} and 2856 cm^{-1} assigning to the C-H stretching adsorptions are visible, indicating TC-2 on the surface of BT. Two peaks at 1092 cm^{-1} and 1045 cm^{-1} can be ascribed to the asymmetric and symmetric stretching modes of P-O-M (M = surface metal),[14, 33, 34] which further proves that TC-2 is bound to the BT surface through the coupling of phosphoric ligands with surface metal of BT particles.

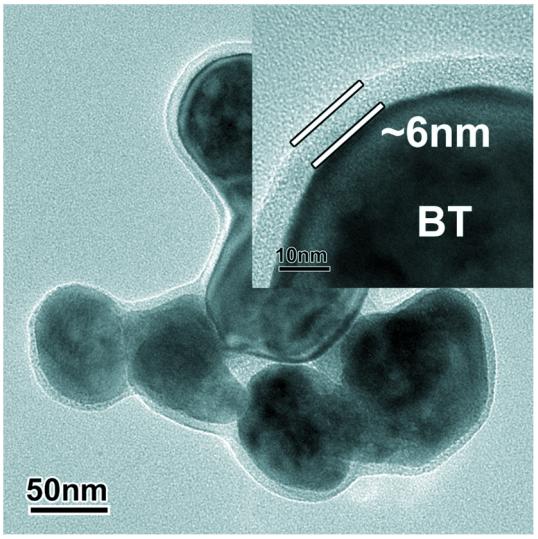

Fig. 2 TEM images for TC-2 modified BT particles.

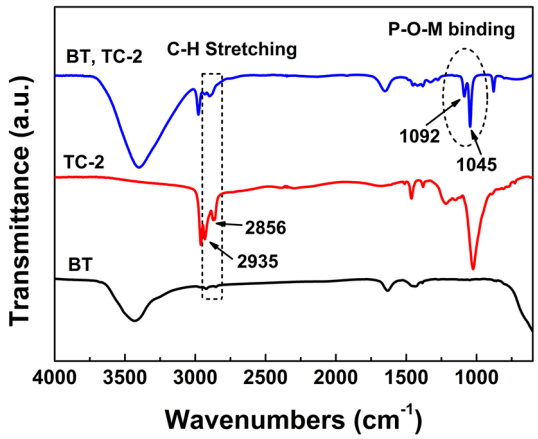

Fig. 3 FT-IR transmission spectra for untreated BT, TC-2, and BT treated with TC-2.

The XRD patterns of BT and BT@ST powders are given in Fig. 4. It is shown that the BT powder is of pure pseudocubic perovskite structure, which is evidenced by the strong diffraction peaks corresponding to JCPDS NO. 05-0626 with no visible signal of secondary phases observed. After coated with ST, the diffraction pattern is almost identical to that of before except for a small peak observed at around 25°, which can be ascribed to {111} faces of the by-product $SrCO_3$ (JCPDS NO. 05-0418) due to the reaction of CO_2 in the atmosphere with the unreacted $Sr(OH)_2$ during crystallization.[35] TGA/DSC measurement in air is conducted in order to investigate the thermal behaviour of the as-fabricated BT@ST powder. As shown in Fig. 5, there are three stages of obvious weight loss in the TGA curve. The first stage below 277 °C is caused by the desorption of the adsorbed water as well as the removal of the solvent. The second stage between 277-584 °C suffers from a significant weight loss by 3.16%, which is assigned to the burnout of TEG as reflected by a strong exothermic peak at 329 °C in the DSC curve. The final stage above 584 °C is due to the loss of chemically bonded hydroxyl

(OH$^-$) groups and partially the carbonic residues.[36-38] The total weight loss is 8.17%.

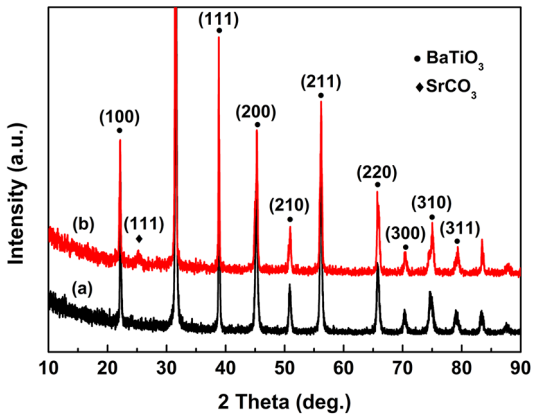

Fig. 4 XRD patterns for the BT (a) and BT@ST (b) powders.

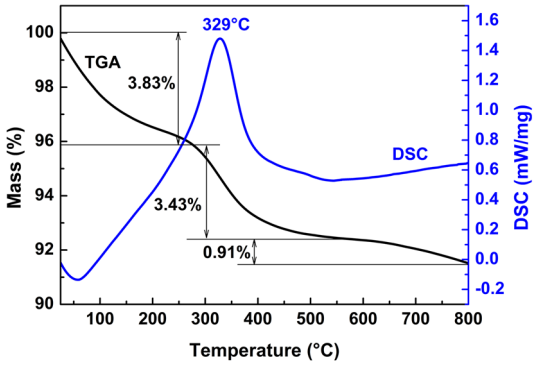

Fig. 5 TGA/DSC curve for the BT@ST powders.

Evidence of the growth of a ST satellite shell on the BT cores is directly provided by SEM and TEM observations. Fig. 6a and Fig. 6b show that the surface of the original BT is rather smooth while the surface of coated BT particles turns rough because of the decoration of ST particles. TEM image (Fig. 6c) has revealed that the ST particles are of cubic shape and are grown on the surface of the BT particles with a narrow grain size distribution of 4-10 nm. Single crystallinity of the ST coatings is confirmed by the well-oriented lattice fringes of 0.283 nm pertaining to {110} planes of $SrTiO_3$ from the HR-TEM image (Fig. 6d). The inserted SAED pattern verifies that most of the ST nanocrystals in the coating layer are randomly oriented, which is similar to the results found by Buscaglia, *et al.*[30] Microstructures for the sintered BT and BT@ST ceramics are illustrated in Fig. 6e and Fig. 6f, respectively. The Sr peak in the inset of Fig 6f is distinct due to the existence of ST nanocubes encapsulated on the BT particles, whereas EDS pattern in the inset of Fig. 6e indicates pure BT with the absence of ST treatment. It is interesting that the average grain size of the BT@ST ceramic is remarkably supressed to ~200 nm; nevertheless, the grains of the pure BT sintered at the same condition exceed 2 μm. The reduction of grain size is favorable for energy storage in that smaller grain sizes are generally associated with lower leakage current and higher voltage withstanding ability.[39]

Dielectric temperature behaviors at various frequencies were measured for the as-sintered bulk ceramics with the BT@ST powders. Fig.7a shows quite high dielectric constant (above 1800) over a wide temperature range from 215 K to 350 K at 1 KHz, and that the dielectric constant maximum shifts about 15 K towards higher temperatures with increasing frequency. The curie peaks are rather flattened and broadened, exhibiting frequency dependent dielectric dispersion similar to typical relaxor ferroelectrics. In addition, higher loss tangent for higher frequency, being a kind of fingerprint for relaxor behavior, can also be observed in Fig. 7b. With the assumption that the dynamics of the dipolar clusters are initiated above a finite freezing temperature, T_f, the Volgel-Fulcher (VF) model[40-43] has been adopted to fit the frequency dispersion of the permittivity or loss tangent data. This model is expressed by Equation (1)

$$f = f_0 \exp\left[-E_a / k_B (T_{\max} - T_f)\right] \qquad (1)$$

where f is the experimental frequency of the permittivity maximum, f_0 is the Debye frequency, E_a is the activation energy, k_B is Boltzmann's constant, and $T_{\max}$ here is the permittivity maximum. Nonlinear fitting of the VF model was applied to the permittivity data with good agreement ($R^2 > 0.99$) obtained, as shown in the inset of Fig. 7a. Key parameters, namely, the activation energy, the Debye frequency, and the freezing temperature value are thus found to be 0.0202±0.008 eV, 3.2 × 10^9 Hz, 292±3 K, respectively, which are in good conformity with those of the relaxor capacitor reported by other researchers.[3]

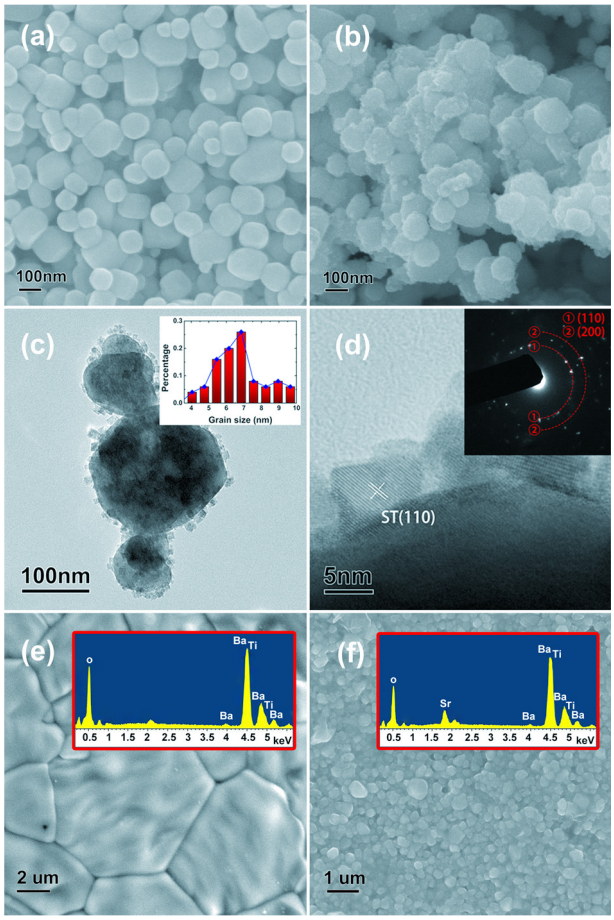

Fig. 6 (a) SEM image of the original BT powders. (b) SEM image of the coated BT powders. (c) TEM image of the BT@ST powders. The inset shows the size distribution of the ST particles. (d) High-resolution TEM image of the BT@ST powders. The inset is the SEAD pattern. (e) SEM image of the sintered BT pellet. (f) SEM image of the sintered BT@ST pellet. The insets in (e) and (f) are the EDS patterns for the sintered BT and BT@ST pellets, respectively.

To study the origin of the relaxation behavior for the as-fabricated ceramic, XRD and EDS characterizations were carried out. As demonstrated in the XRD patterns in Fig.8a and the maginification in Fig. 8b, evident peak splitting at $2\theta \sim 45^{o}$ can be witnessed, demonstrating good tetragonality for the pure BT ceramic sample, whereas the diffraction peaks for the BT@ST ceramic sample become merged, forming pseudocubic perovskite structure. The peaks of the BT@ST ceramic shift to higher degrees contrasted with those of the original BT ceramic, which is because of the lattice shrinkage originated from the introduction of Sr element in place of Ba element.[44] Fig. 9 illustrates the EDS line scanning analysis of Sr element from point A to point B of the BT@ST ceramic sample. The concentration of Sr changes gradually from grain boundary to grain core center to form a local compositionally graded structure, which gives rise to a distribution of the Curie temperature (Tc), and consequently, flattened and broadened temperature dependent dielectric characteristics,[45] and is also responsible for the dielectric relaxation behavior believed to be caused by in-built polarization effect rather than space charge effects[3] as shown in Fig. 7.

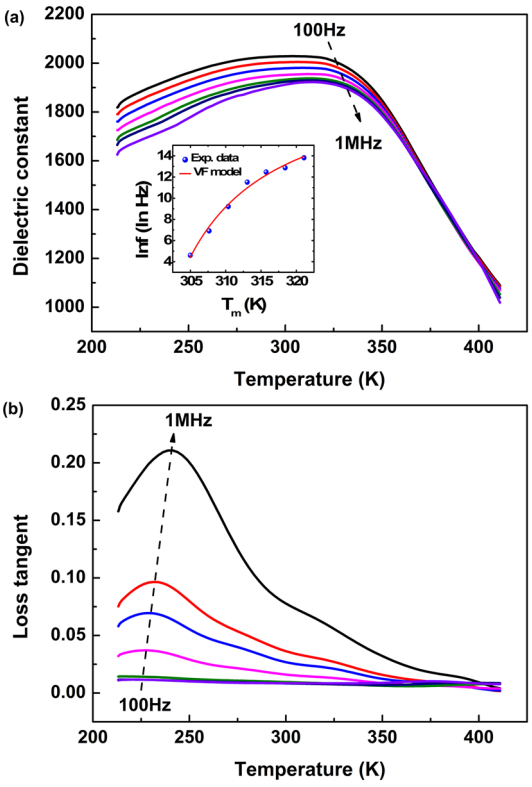

Fig. 7 Temperature and frequency dependent (a) dielectric constant and (b) loss tangent of the BT@ST bulk ceramic. The inset in (a) shows the nonlinear Vogel-Fulcher fit of the dielectric data.

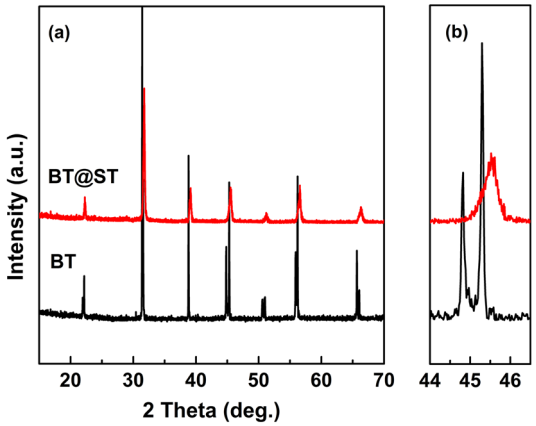

Fig. 8 XRD patterns for the BT and BT@ST bulk ceramics. (a) full spectra; (b) detailed patterns at 2 theta from 44^{o} to 46.5^{o}.

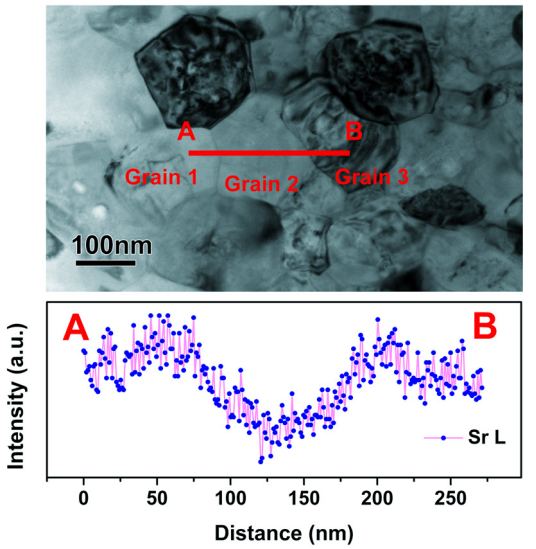

Fig. 9 EDS line scanning analysis of Sr element in the BT@ST ceramic.

Under the effect of applied electric field E, the macroscopic dielectric response of dielectrics can be described with the parameter ε named as dielectric constant or permittivity, as shown in Equation (2)

$$D = \varepsilon_0 \varepsilon E \qquad (2)$$

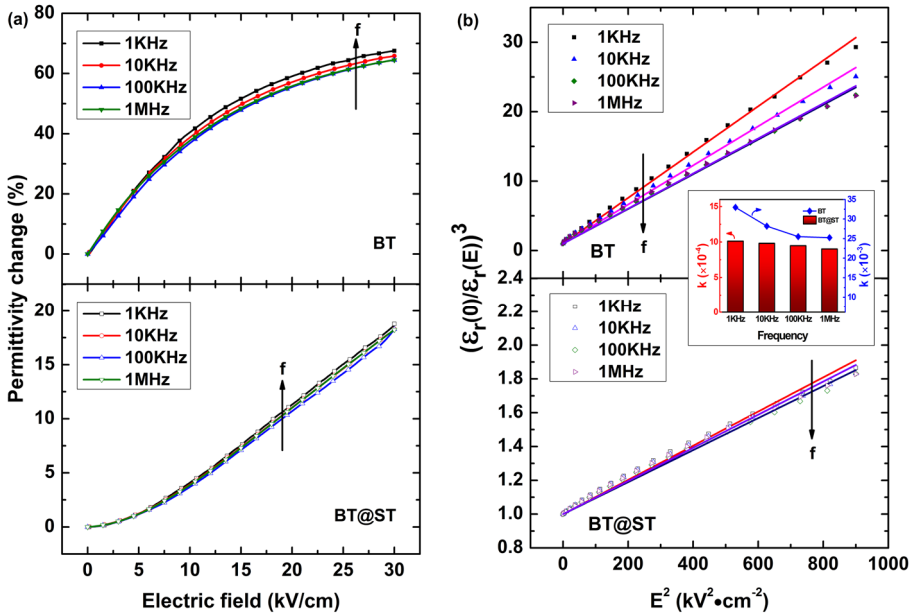

Fig. 10. Electric field dependence of permittivity change (a), and nonlinear fit of the Johnson's model (b) at various frequencies for the BT and BT@ST ceramics. The inset in (b) shows the frequency dependent *k* values for the BT and BT@ST ceramics.

where D is the electric displacement, and ε_0 is the permittivity in vacuum. For isotropic dielectrics, the directions of D and E are the same such that ε is a scalar. Nevertheless, for most dielectrics, the direction of D is experimentally observed to be different from that of E , that is, these dielectrics are anisotropic. For anisotropic dielectrics, the dielectric response has to be expressed by tensors, as shown in Equation (3)

$$D_\alpha = \varepsilon_0 \varepsilon_{\alpha\beta} E_\beta, \quad \alpha, \beta = 1,2,3 \qquad (3)$$

where $\varepsilon_{\alpha\beta}$ is a tensor in Einstein notation. With higher order tensors taken into account, Equation (3) can be rewritten as

$$D_\alpha = \varepsilon_0 \varepsilon_{\alpha\beta} E_\beta + \varepsilon_0 \varepsilon_{\alpha\beta\gamma} E_\beta E_\gamma + \varepsilon_0 \varepsilon_{\alpha\beta\gamma\delta} E_\beta E_\gamma E_\delta + \ldots \qquad (4)$$

Usually, for most insulating dielectrics, the values of higher order tensors, *i.e.*, $\varepsilon_{\alpha\beta\gamma}$ and $\varepsilon_{\alpha\beta\gamma\delta}$, *etc.* are quite small and neglectable, while as the electric field is elevated to a sufficient large value, the higher order terms will come into effect, exhibiting dielectric nonlinearity which can be known as the nonlinear decrease of the dielectric constant as a function of applied electric field. As for ferroelectric materials, the high dielectric nonlinearity is one of the weak characteristics that restrict their utilization in high power or high energy density capacitors. To retrieve exact dielectric nonlinearity behaviors of the BT and BT@ST bulk ceramic systems, DC bias performances under the C-V mode were carried out. The dielectric nonlinearity is depicted as the permittivity change along with the increase of applied electric field, which is calculated using Equation (5)

$$\text{Permittivity change} = \frac{\varepsilon_r(0) - \varepsilon_r(E)}{\varepsilon_r(0)} \times 100\% \qquad (5)$$

where $\varepsilon_r(0)$ and $\varepsilon_r(E)$ are the relative permittivity under an applied electric field bias of zero and E , respectively. Fig. 10a exhibits the electric field dependence of permittivity change at several separate frequencies of the BT and BT@ST ceramics. With the electric field increasing from 0 kV/cm to 30 kV/cm, the permittivity of the BT ceramic is dramatically suppressed by 67.56%, 65.83%, 64.51% and 64.47% for the probing frequencies of 1KHz, 10 KHz, 100 KHz and 1 MHz, respectively; while for the BT@ST ceramic, the permittivity change is only 18.78%, 18.29%, 18.27% and 18.23% for frequencies of 1KHz, 10 KHz, 100 KHz and 1 MHz, correspondingly. The nonlinearity of the BT@ST ceramic is to a large extent weakened compared to the pure BT ceramic as evidenced by the less than one third smaller decrease in the permittivity changes for all the four separate probing frequencies, which may be owing to the reduced grain size[46] and the soft mode hardening due to the substitution of Ba with Sr.[47] The slightly negative correlation of the permittivity change with the probing frequency observed for both the BT and BT@ST ceramic may arise from some slow relaxation mechanism.[48] Based on Devonshire's phenomenological theory, the Johnson's model[39, 49-51] has been applied to well describe the nonlinear dielectric behaviors under external bias field, which is expressed as Equation (6)

$$\frac{\varepsilon_r(E)}{\varepsilon_r(0)} = \frac{1}{\left(1 + kE^2\right)^{1/3}} \qquad (6)$$

where $k = \alpha\varepsilon_r(0)^3$ can be recognized as a parameter to describe the dielectric nonlinearity, and α is the coefficient related to the levels of anharmonic interactions among Ti^{4+} ions[52]. By changing Equation (6) into the form of $(\varepsilon_r(0)/\varepsilon_r(E))^3$ *versus* E^2, linear regressions of this model were conducted for the BT and BT@ST ceramics with good agreement attained ($R^2 > 0.99$ for all fittings), as indicated in the results shown in Fig. 10b. The inset of Fig. 10b demonstrates the frequency dependence of the parameter k. With the increase of the frequency value, both the k values for the BT and BT@ST ceramics reduce, and furthermore, what can be noticed is that the k value of the BT ceramic with respect to the corresponding frequency is over an order higher than that of the BT@ST ceramic, indicating a weakened nonlinearity for the BT@ST ceramic and that the parameter k is a practical metric to benchmark the dielectric nonlinearity.

Electric conductivity of dielectrics in service may cause energy loss, generate heat, and eventually lead to failure or breakdown. Leakage current properties under strong applied voltage were carried out with the aim to evaluate the effect of the electric insulation performance of the ST coating treatment for the BT ceramic. Fig. 11a displays the current density-time characteristics at room temperature and 30 kV/cm for the BT and BT@ST samples. As is demonstrated, the current density of the BT@ST ceramic is over an order higher than that of the BT ceramic, which indicates that the BT@ST ceramic has better insulation ability and is capable of enduring higher electric field. The leakage current is found to decay along with time, which is supposed to be in obedience to the Curie-von Schweidler equation[53-55] associated with mechanisms of space charge trapping, relaxation time distribution and electric charge hopping, as presented in Equation (7)

$$J = J_s + J_0 \times t^{-n} \quad (7)$$

where J_s is the steady-state current density, J_0 is a fitting constant, t is the relaxation time in seconds, and n is the slope of the log-log plot. Least square fittings were applied to the experimental current density for the BT and BT@ST ceramics. Fig. 11a shows that a good agreement is achieved between the experimental results and the model values. The J_s values obtained for the BT sample and BT@ST sample are 5.38×10^{-6} A/cm^2 and 4.73×10^{-7} A/cm^2, respectively. Compared to the pure BT ceramic, the value of J_s of the BT@ST ceramic is remarkably reduced by about an order, demonstrating stronger insulation ability of the BT@ST ceramic due to the ST coatings.

As for high power or energy storage usage, breakdown strength of the dielectrics is one of the key characteristics measuring the performance of the material, for which the Weibull analysis[56] of the dielectric breakdown strength data obtained at room temperature is adopted. The cumulative distribution function using two parameters is defined as Equation (8)

$$P = 1 - \exp\left[-\left(\frac{E}{\alpha}\right)^{\beta}\right] \quad (8)$$

where P is the cumulative probability of failure, α, the so-called characteristic breakdown strength, is a scale parameter representing the breakdown strength at the cumulative failure probability of 63.2%, β is a shape parameter that indicates the dispersion of the data, and E is the threshold below which no breakdown occurs. For every sample with specific value of E, P is estimated by Equation (9) as

$$P = \frac{i}{n+1} \quad (9)$$

where i is the index number of which the corresponding E value ranks the ith in an ascending order among the breakdown strength data and n here represents the total number of data points. The Weibull distribution was fitted through linear regression of $\ln(-\ln(1-P))$ *versus* $\ln E$ and good correlations were reached, as manifested in Fig. 11b. The values of Weibull moduli α and β obtained for BT ceramic are 11.3 kV/mm and 3.37, respectively; whilst the two parameters for the BT@ST ceramic are correspondingly 21.8 kV/mm and 3.64. The value of the shape parameter β for both ceramic formula are more than three, providing a high reliability of the analysis.[57] The value of the scale parameter α for the BT@ST ceramic is almost double of that for the BT ceramic, indicating that the ST cubes precipitating on the BT particles is favorable for the enhancement of breakdown strength.

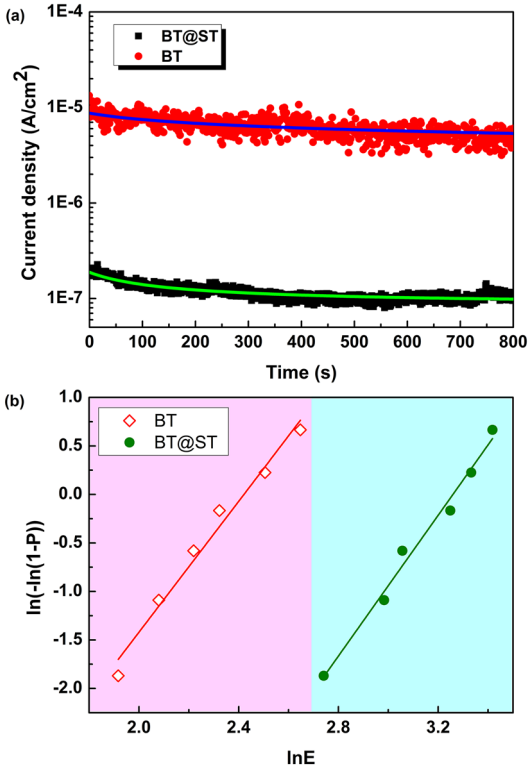

Fig. 11. Time-dependent leakage current density (a) and Weibull distribution (b) for the BT and BT@ST ceramics.

Polarization hysteresis loops obtained at various electric fields for BT and BT@ST ceramics are exhibited in Fig. 12a. The hysteresis loops for the BT@ST ceramic are much slimmer than those for the BT ceramic, which is owing to the relaxor behavior of the BT@ST ceramic that microdomains, or polar nanoregions (PNRs) rather than macrodomains, or ordinary ferroelectric domains exist over a wide temperature range in the vicinity of phase transition.[58-60] Due to their smaller characteristic size, here ~ 9.5 nm of an average size as demonstrated in the inset of Fig.12a, the PNRs are more susceptive to external electric field than macroscopic domains, and frequently lead to slimmer loops. The slope of the curve, related to the dielectric constant, is observed to be lower of the BT@ST ceramic than that of the BT ceramic, which may be as a consequence of the fact that the PNRs with smaller size are less polarizable than the larger macroscopic domains. As can be noticed, the remanent polarization and the coercive field of the BT@ST ceramic are suppressed compared with those of the BT ceramic, which is technologically meaningful for energy storage because a low remanent polarization and coercive field are generally associated with low energy loss, as indicated in the small area of the hysteresis loop. For practical application, both the two parameters, namely, the energy storage density and the energy efficiency should be taken into consideration. It seems that the BT ceramic has larger polarization favorable for energy storage, but yet simultaneously has higher nonlinearity and bigger hysteresis loop area which deteriorates energy utilization efficient in comparison with the BT@ST ceramic. Under this circumstance, the energy storage density and energy efficiency were further examined by calculation using Equation (10) and Equation (11), respectively.

$$\text{Energy storage} = \int_{P_r}^{P_m} E\mathrm{d}P \qquad (10)$$

and

$$\text{Energy efficiency} = \frac{A_{\mathrm{I}}}{A_{\mathrm{I}} + A_{\mathrm{II}}} \times 100\% \qquad (11)$$

where P_r is the remanent polarization, P_m is the maximum polarization with respect to the maximum experimental electric field, A_{I} is equal to the energy storage, and A_{II} represents the closed area of the hysteresis loop. All the integrations are taken numerically using the trapezoidal method. Fig. 12b shows the energy storage density at various applied electric fields for the BT and BT@ST ceramics. At lower fields (here less than ~22.5 kV/cm), the energy storage density for the BT ceramic is higher which can be owing to its higher polarization. However, as the electric field gradually increases, the situation is reversed, that is, the energy storage density for the BT@ST ceramic exceeds that for the BT ceramic and the discrepancy enlarges with further elevation of the electric field. For instance, at 47 kV/cm, the energy storage density for the BT@ST ceramic is 0.22 J/cm^3, which is approximately 1.6 times of that of 0.14 J/cm^3 for the BT ceramic. The reason why the BT@ST ceramic possesses higher energy storage at elevated electric fields can be convinced by its lower nonlinear behavior as illustrated in the hysteresis loops shown in Fig. 12a and in the DC bias properties confirmed in Fig. 10. As given in the inset of Fig. 12b, the energy efficiency for the BT@ST ceramic is approaching 90% at all the measuring electric fields, far surpassing that for the BT ceramic which is only as low as around 55%. The high energy efficiency of the BT@ST ceramic is directly verified from the small area of the hysteresis loops, and may be as a result of the effect of the PNRs mentioned hereinbefore.

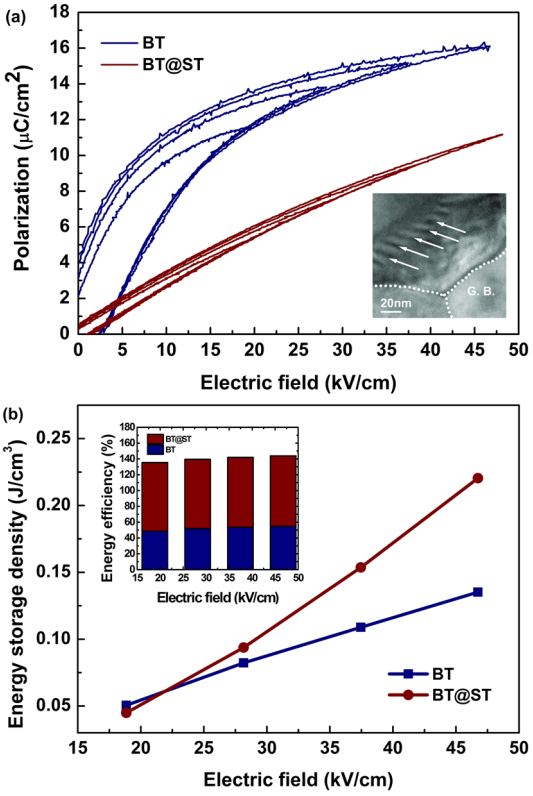

Fig. 12. Polariation-electric field (P-E) hysteresis loops (a) and energy storage density (b) for the BT and BT@ST ceramics. The inset in (a) indicated by arrows shows the domain patterns for the BT@ST ceramic where G.B. is short for grain boundary, and the inset in (b) shows the energy efficiency for the BT and BT@ST ceramics.

Conclusions

In summary, core-satellite structured BT@ST assemblies were successfully fabricated *via* a facile sol-precipitation method with the titanate coupling agent TC-2 for surface modification. The resulting BT@ST bulk ceramics using the as-synthesized powders were prepared through conventional sintering. Experimental results of this work show that the ST satellite shell is composed of well crystallized nanocubes with a narrow size distribution of 4-10 nm which are grown on the surface of the BT particles. In comparison with the original BT ceramic, the BT@ST ceramic exhibits superior electric and dielectric performances manifested in that the dielectric nonlinearity is weakened to < 1/3, the leakage current is suppressed by about

an order and the dielectric breakdown strength is to a large extent improved, resulting in an enhanced energy storage density (0.22 J/cm^3 at 47 kV/cm, approximately 1.6 times of that of the pure BT ceramic) and a high energy efficiency approaching 90%, which can be as a consequence of the significant suppression of grain size and the formation of local compositionally graded relaxor ferroelectric capacitor.

Acknowledgements

The work was supported by Ministry of Sciences and Technology of China through National Basic Research Program of China (973 Program 2015CB654604), National Natural Science Foundation of China for Creative Research Groups (Grant No.51221291), National Natural Science Foundation of China (Grant No. 51272123), and also supported by CBMI Construction Co., Ltd.

Notes and references

State Key Laboratory of New Ceramics and Fine Processing, School of Materials Science and Engineering, Tsinghua University, Beijing 100084, China. E-mail: wxh@tsinghua.edu.cn; llt-dms@mail.tsinghua.edu.cn.

† Footnotes should appear here. These might include comments relevant to but not central to the matter under discussion, limited experimental and spectral data, and crystallographic data.
Electronic Supplementary Information (ESI) available: [details of any supplementary information available should be included here]. See DOI: 10.1039/b000000x/

1 M. Winter and R. J. Brodd, *Chem. Rev.*, 2004, **104**, 4245-4270.
2 K. Han, Q. Li, Z. Chen, M. R. Gadinski, L. Dong, C. Xiong and Q. Wang, *J. Mater. Chem. C*, 2013, **1**, 7034-7042.
3 N. Ortega, A. Kumar, J. F. Scott, D. B. Chrisey, M. Tomazawa, S. Kumari, D. G. B. Diestra and R. S. Katiyar, *J. Phys.: Condens. Matter*, 2012, **24**, 445901.
4 T. M. Correia, M. McMillen, M. K. Rokosz, P. M. Weaver, J. M. Gregg, G. Viola, M. G. Cain and G. L. Brennecka, *J. Am. Ceram. Soc.*, 2013, **96**, 2699-2702.
5 L. Xie, X. Huang, B.-W. Li, C. Zhi, T. Tanaka and T. Jiang, *PCCP*, 2013, **15**, 17560-17569.
6 H. Ogihara, C. A. Randall and S. Trolier‐McKinstry, *J. Am. Ceram. Soc.*, 2009, **92**, 110-118.
7 X. Hao, *J. Adv. Dielectr.*, 2013, **03**, 1330001.
8 K. M. Slenes, P. Winsor, T. Scholz and M. Hudis, *IEEE Trans. Magn.*, 2001, **37**, 324-327.
9 X. Hao, Y. Wang, L. Zhang, L. Zhang and S. An, *Appl. Phys. Lett.*, 2013, **102**, 163903.
10 B. Chu, X. Zhou, K. Ren, B. Neese, M. Lin, Q. Wang, F. Bauer and Q. M. Zhang, *Science*, 2006, **313**, 334-336.
11 L. Zhu and Q. Wang, *Macromolecules*, 2012, **45**, 2937-2954.
12 Y. Wang, X. Zhou, Q. Chen, B. Chu and Q. Zhang, *IEEE Trans. Dielectr. Electr. Insul.*, 2010, **17**, 1036-1042.
13 J. Li, S. I. Seok, B. Chu, F. Dogan, Q. Zhang and Q. Wang, *Adv. Mater.*, 2009, **21**, 217-221.
14 P. Kim, N. M. Doss, J. P. Tillotson, P. J. Hotchkiss, M.-J. Pan, S. R. Marder, J. Li, J. P. Calame and J. W. Perry, *ACS Nano*, 2009, **3**, 2581-2592.
15 K. Yang, X. Huang, Y. Huang, L. Xie and P. Jiang, *Chem. Mater.*, 2013, **25**, 2327-2338.
16 P. Hu, Y. Shen, Y. Guan, X. Zhang, Y. Lin, Q. Zhang and C.-W. Nan, *Adv. Funct. Mater.*, 2014, **24**, 3172-3178.
17 Y. Zhang, J. Huang, T. Ma, X. Wang, C. Deng and X. Dai, *J. Am. Ceram. Soc.*, 2011, **94**, 1805-1810.
18 J. Ge, X. Dong, Y. Chen, F. Cao and G. Wang, *Appl. Phys. Lett.*, 2013, **102**, 142905.
19 M. Ye, Q. Sun, X. Chen, Z. Jiang and F. Wang, *J. Am. Ceram. Soc.*, 2011, **94**, 3234-3236.
20 Z. Hu, B. Ma, S. Liu, M. Narayanan and U. Balachandran, *Ceram. Int.*, 2014, **40**, 557-562.
21 K. Yao, S. Chen, M. Rahimabady, M. S. Mirshekarloo, S. Yu, F. E. H. Tay, T. Sritharan and L. Li, *IEEE Trans. Ultrason., Ferroelectr., and Freq. Control*, 2011, **58**, 1968-1974.
22 D.-K. Kwon and M. H. Lee, *IEEE Trans. Ultrason., Ferroelectr., and Freq. Control*, 2012, **59**, 1894-1899.
23 T. Wang, X. Wei, Q. Hu, L. Jin, Z. Xu and Y. Feng, *Mater. Sci. Eng., B*, 2013, **178**, 1081-1086.
24 X. Wang, Y. Zhang, X. Song, Z. Yuan, T. Ma, Q. Zhang, C. Deng and T. Liang, *J. Eur. Ceram. Soc.*, 2012, **32**, 559-567.
25 V. S. Puli, D. K. Pradhan, B. C. Riggs, D. B. Chrisey and R. S. Katiyar, *Integr. Ferroelectr.*, 2014, **157**, 139-146.
26 V. S. Puli, A. Kumar, D. B. Chrisey, M. Tomozawa, J. F. Scott and R. S. Katiyar, *J. Phys. D: Appl. Phys.*, 2011, **44**, 395403.
27 G. Zhao, Y. Li, H. Liu, J. Xu, H. Hao, M. Cao and Z. Yu, *J. Ceram. Process. Res.*, 2012, **13**, 310-314.
28 Q.-G. Hu, Z.-Y. Shen, Y.-M. Li, Z.-M. Wang, W.-Q. Luo and Z.-X. Xie, *Ceram. Int.*, 2014, **40**, 2529-2534.
29 Z. Wang, M. Cao, Z. Yao, G. Li, Z. Song, W. Hu, H. Hao, H. Liu and Z. Yu, *Ceram. Int.*, 2014, **40**, 929-933.
30 M. T. Buscaglia, M. Viviani, Z. Zhao, V. Buscaglia and P. Nanni, *Chem. Mater.*, 2006, **18**, 4002-4010.
31 E. Müller, Č. Drašar, J. Schilz and W. A. Kaysser, *Mater. Sci. Eng., A*, 2003, **362**, 17-39.
32 T. Šetinc, M. Spreitzer, Š. Kunej, J. Kovač and D. Suvorov, *J. Am. Ceram. Soc.*, 2013, **96**, 3511-3517.
33 P. Kim, S. C. Jones, P. J. Hotchkiss, J. N. Haddock, B. Kippelen, S. R. Marder and J. W. Perry, *Adv. Mater.*, 2007, **19**, 1001-1005.
34 S. A. Paniagua, P. J. Hotchkiss, S. C. Jones, S. R. Marder, A. Mudalige, F. S. Marrikar, J. E. Pemberton and N. R. Armstrong, *J. Phys. Chem. C*, 2008, **112**, 7809-7817.
35 Y. Hao, X. Wang and L. Li, *Nanoscale*, 2014, **6**, 7940-7946.
36 Y. Gao, V. V. Shvartsman, A. Elsukova and D. C. Lupascu, *J. Mater. Chem.*, 2012, **22**, 17573-17583.
37 D. F. K. Hennings, C. Metzmacher and B. S. Schreinemacher, *J. Am. Ceram. Soc.*, 2001, **84**, 179-182.
38 C. Pithan, Y. Shiratori, R. Waser, J. Dornseiffer and F.-H. Haegel, *J. Am. Ceram. Soc.*, 2006, **89**, 2908-2916.
39 Z. Song, H. Liu, S. Zhang, Z. Wang, Y. Shi, H. Hao, M. Cao, Z. Yao and Z. Yu, *J. Eur. Ceram. Soc.*, 2014, **34**, 1209-1217.
40 H. Vogel, *Phys. Z.*, 1921, **22**, 645-646.
41 G. S. Fulcher, *J. Am. Ceram. Soc.*, 1925, **8**, 339-355.

42 D. Viehland, S. J. Jang, L. E. Cross and M. Wuttig, *J. Appl. Phys.*, 1990, **68**, 2916-2921.
43 C. Ang, Z. Yu and Z. Jing, *Phys. Rev. B*, 2000, **61**, 957-961.
44 V. V. Lemanov, E. P. Smirnova, P. P. Syrnikov and E. A. Tarakanov, *Phys. Rev. B*, 1996, **54**, 3151-3157.
45 T. R. Armstrong and R. C. Buchanan, *J. Am. Ceram. Soc.*, 1990, **73**, 1268-1273.
46 T. Sun, X. Wang, H. Wang, Z. Cheng, X. Zhang and L. Li, *J. Am. Ceram. Soc.*, 2010, **93**, 3808-3813.
47 J. Zhang, J. Zhai, X. Chou, J. Shao, X. Lu and X. Yao, *Acta Mater.*, 2009, **57**, 4491-4499.
48 X. Wei and X. Yao, *Mater. Sci. Eng., B*, 2003, **99**, 74-78.
49 K. M. Johnson, *J. Appl. Phys.*, 1962, **33**, 2826.
50 L. P. Curecheriu, L. Mitoseriu and A. Ianculescu, *J. Alloys Compd.*, 2009, **482**, 1-4.
51 A. Tkach, P. M. Vilarinho and A. L. Kholkin, *J. Appl. Phys.*, 2007, **101**, 084110.
52 X. Liang, W. Wu and Z. Meng, *Mater. Sci. Eng., B*, 2003, **99**, 366-369.
53 A. K. Jonscher, *Dielectric Relaxation in Solids*, Chelsea Dielectric Press, London, 1983.
54 B. Ma, D.-K. Kwon, M. Narayanan and U. B. Balachandran, *J. Phys. D: Appl. Phys.*, 2008, **41**, 205003.
55 L. Zhang, X. Hao, L. Zhang, J. Yang and S. An, *J. Mater. Sci.: Mater. Electron.*, 2013, **24**, 3830-3835.
56 D. Wu, J. Zhou and Y. Li, *J. Eur. Ceram. Soc.*, 2006, **26**, 1099-1105.
57 A. R. Blythe and D. Bloor, *Electrical properties of polymers*, Cambridge University Press, 2005.
58 A. A. Bokov and Z.-G. Ye, *J. Mater. Sci.*, 2006, **41**, 31-52.
59 W. Kleemann, *J. Mater. Sci.*, 2006, **41**, 129-136.
60 L. Jin, F. Li and S. Zhang, *J. Am. Ceram. Soc.*, 2014, **97**, 1-27.

Facile sol-precipitation fabrication of core-satellite BaTiO3@SrTiO3 assemblies for local compositionally graded capacitor